Biomedical Optics EXPRESS

Intraoperative measurement of bowel oxygen saturation using a multispectral imaging laparoscope

Neil T. Clancy,[1,2,*] Shobhit Arya,[1] Danail Stoyanov,[3] Mohan Singh,[1,2] George B. Hanna,[1] and Daniel S. Elson[1,2]

[1]*Department of Surgery and Cancer, Imperial College London, SW7 2AZ, UK*
[2]*Hamlyn Centre for Robotic Surgery, Institute of Global Health Innovation, Imperial College London, SW7 2AZ, UK*
[3]*Centre for Medical Image Computing, Department of Computer Science, University College London, WC1E 6BT, UK*
**n.clancy@imperial.ac.uk*

Abstract: Intraoperative monitoring of tissue oxygen saturation (StO_2) has potentially important applications in procedures such as organ transplantation or colorectal surgery, where successful reperfusion affects the viability and integrity of repaired tissues. In this paper a liquid crystal tuneable filter-based multispectral imaging (MSI) laparoscope is described. Motion-induced image misalignments are reduced, using feature-based registration, before regression of the tissue reflectance spectra to calculate relative quantities of oxy- and deoxyhaemoglobin. The laparoscope was validated *in vivo*, during porcine abdominal surgery, by making parallel MSI and blood gas measurements of the small bowel vasculature. Ischaemic conditions were induced by local occlusion of the mesenteric arcade and monitored using the system. The MSI laparoscope was capable of measuring StO_2 over a wide range (30-100%) with a temporal error of ± 7.5%. The imager showed sensitivity to spatial changes in StO_2 during dynamic local occlusions, as well as tracking the recovery of tissues post-occlusion.

OCIS codes: (110.4234) Multispectral and hyperspectral imaging; (170.0170) Medical optics and biotechnology; (170.1610) Clinical applications; (170.2150) Endoscopic imaging; (170.2655) Functional monitoring and imaging; (170.6510) Spectroscopy, tissue diagnostics.

References and links

1. H. Birke-Sorensen, "Detection of postoperative intestinal ischemia in small bowel transplants," J. Transplant. **2012**, 970630 (2012).
2. N. J. Crane, S. W. Huffman, M. Alemozaffar, F. A. Gage, I. W. Levin, and E. A. Elster, "Evidence of a heterogeneous tissue oxygenation: renal ischemia/reperfusion injury in a large animal model," J. Biomed. Opt. **18**(3), 035001 (2013).
3. A. Alves, Y. Panis, D. Trancart, J.-M. Regimbeau, M. Pocard, and P. Valleur, "Factors associated with clinically significant anastomotic leakage after large bowel resection: multivariate analysis of 707 patients," World J. Surg. **26**(4), 499–502 (2002).
4. A. Matsui, J. H. Winer, R. G. Laurence, and J. V. Frangioni, "Predicting the survival of experimental ischaemic small bowel using intraoperative near-infrared fluorescence angiography," Br. J. Surg. **98**(12), 1725–1734 (2011).
5. G. Lu and B. Fei, "Medical hyperspectral imaging: a review," J. Biomed. Opt. **19**(1), 010901 (2014).
6. M. G. Sowa, J. R. Payette, M. D. Hewko, and H. H. Mantsch, "Visible-near infrared multispectral imaging of the rat dorsal skin flap," J. Biomed. Opt. **4**(4), 474–481 (1999).
7. M. A. Ilias, E. Häggblad, C. Anderson, and E. G. Salerud, "Visible, hyperspectral imaging evaluating the cutaneous response to ultraviolet radiation," Proc. SPIE **6441**, 644103 (2007).
8. S. P. Nighswander-Rempel, R. Anthony Shaw, J. R. Mansfield, M. Hewko, V. V. Kupriyanov, and H. H. Mantsch, "Regional variations in myocardial tissue oxygenation mapped by near-infrared spectroscopic imaging," J. Mol. Cell. Cardiol. **34**(9), 1195–1203 (2002).

#241963 Received 18 Sep 2015; revised 21 Sep 2015; accepted 27 Sep 2015; published 30 Sep 2015

9. B. S. Sorg, B. J. Moeller, O. Donovan, Y. Cao, and M. W. Dewhirst, "Hyperspectral imaging of hemoglobin saturation in tumor microvasculature and tumor hypoxia development," J. Biomed. Opt. **10**(4), 044004 (2005).
10. K. J. Zuzak, M. T. Gladwin, R. O. I. Cannon 3rd, and I. W. Levin, "Imaging hemoglobin oxygen saturation in sickle cell disease patients using noninvasive visible reflectance hyperspectral techniques: effects of nitric oxide," Am. J. Physiol. Heart Circ. Physiol. **285**(3), H1183–H1189 (2003).
11. J. C. Ramella-Roman and S. A. Mathews, "Spectroscopic measurements of oxygen saturation in the retina," IEEE Sel. Top. Quantum Electron. **13**(6), 1697–1703 (2007).
12. D. Stoyanov, A. Rayshubskiy, and E. Hillman, "Robust registration of multispectral images of the cortical surface in neurosurgery," in *Proceedings of IEEE International Symposium on Biomedical Imaging* (IEEE, 2012), pp. 1643–1646.
13. C. R. Tracy, J. D. Terrell, R. P. Francis, E. F. Wehner, J. Smith, M. Litorja, D. L. Hawkins, M. S. Pearle, J. A. Cadeddu, and K. J. Zuzak, "Characterization of renal ischemia using DLP hyperspectral imaging: a pilot study comparing artery-only occlusion versus artery and vein occlusion," J. Endourol. **24**(3), 321–325 (2010).
14. S. P. Nighswander-Rempel, R. A. Shaw, V. V. Kupriyanov, J. Rendell, B. Xiang, and H. H. Mantsch, "Mapping tissue oxygenation in the beating heart with near-infrared spectroscopic imaging," Vib. Spectrosc. **32**(1), 85–94 (2003).
15. K. J. Zuzak, M. D. Schaeberle, M. T. Gladwin, R. O. I. Cannon 3rd, and I. W. Levin, "Noninvasive determination of spatially resolved and time-resolved tissue perfusion in humans during nitric oxide inhibition and inhalation by use of a visible-reflectance hyperspectral imaging technique," Circulation **104**(24), 2905–2910 (2001).
16. K. J. Zuzak, M. D. Schaeberle, E. N. Lewis, and I. W. Levin, "Visible reflectance hyperspectral imaging: characterization of a noninvasive, in vivo system for determining tissue perfusion," Anal. Chem. **74**(9), 2021–2028 (2002).
17. L. L. Randeberg, E. L. P. Larsen, and L. O. Svaasand, "Characterization of vascular structures and skin bruises using hyperspectral imaging, image analysis and diffusion theory," J. Biophotonics **3**(1-2), 53–65 (2010).
18. H. L. Fu, B. Yu, J. Y. Lo, G. M. Palmer, T. F. Kuech, and N. Ramanujam, "A low-cost, portable, and quantitative spectral imaging system for application to biological tissues," Opt. Express **18**(12), 12630–12645 (2010).
19. S. Wirkert, N. T. Clancy, D. Stoyanov, S. Arya, G. B. Hanna, H.-P. Schlemmer, P. Sauer, D. S. Elson, and L. Maier-Hein, "Endoscopic Sheffield index for unsupervised in vivo spectral band selection," in *Computer-Assisted and Robotic Endoscopy* (Springer, 2014), pp. 110–120.
20. S. Gioux, A. Mazhar, B. T. Lee, S. J. Lin, A. M. Tobias, D. J. Cuccia, A. Stockdale, R. Oketokoun, Y. Ashitate, E. Kelly, M. Weinmann, N. J. Durr, L. A. Moffitt, A. J. Durkin, B. J. Tromberg, and J. V. Frangioni, "First-in-human pilot study of a spatial frequency domain oxygenation imaging system," J. Biomed. Opt. **16**(8), 086015 (2011).
21. K. J. Zuzak, S. C. Naik, G. Alexandrakis, D. Hawkins, K. Behbehani, and E. H. Livingston, "Characterization of a near-infrared laparoscopic hyperspectral imaging system for minimally invasive surgery," Anal. Chem. **79**(12), 4709–4715 (2007).
22. N. T. Clancy, V. Sauvage, S. Saso, D. Stoyanov, D. J. Corless, M. Boyd, D. E. Noakes, G.-Z. Yang, S. Ghaem-Maghami, J. R. Smith, and D. S. Elson, "Registration and analysis of multispectral images acquired during uterine transplantation surgery," in *Biomedical Optics and 3-D Imaging*, OSA Technical Digest (Optical Society of America, 2012), paper. BSu3A.73.
23. N. T. Clancy, S. Saso, D. Stoyanov, V. Sauvage, D. J. Corless, M. Boyd, D. E. Noakes, M.-Y. Thum, S. Ghaem-Maghami, A. D. Smith, and D. S. Elson, "Multispectral imaging of organ viability during uterine transplantation surgery," Proc. SPIE **8935**, 893510 (2014).
24. X. Du, N. T. Clancy, S. Arya, G. B. Hanna, J. Kelly, D. S. Elson, and D. Stoyanov, "Robust surface tracking combining features, intensity and illumination compensation," Int. J. CARS (2015, in press).
25. S. A. Prahl, "Tabulated molar extinction coefficient for hemoglobin in water," http://omlc.ogi.edu/spectra/hemoglobin/summary.html, Accessed June, 2009.
26. P. Verwaerde, C. Malet, M. Lagente, F. de la Farge, and J. P. Braun, "The accuracy of the i-STAT portable analyser for measuring blood gases and pH in whole-blood samples from dogs," Res. Vet. Sci. **73**(1), 71–75 (2002).
27. S. L. Jacques, "Optical properties of biological tissues: a review," Phys. Med. Biol. **58**(11), R37–R61 (2013).
28. M. Kohl, U. Lindauer, G. Royl, M. Kühl, L. Gold, A. Villringer, and U. Dirnagl, "Physical model for the spectroscopic analysis of cortical intrinsic optical signals," Phys. Med. Biol. **45**(12), 3749–3764 (2000).
29. J. Rosenberg, W. E. Dirkes, and H. Kehlet, "Episodic arterial oxygen desaturation and heart rate variations following major abdominal surgery," Br. J. Anaesth. **63**(6), 651–654 (1989).
30. L. J. Hirst, G. A. Ford, G. J. Gibson, and J. A. Wilson, "Swallow-induced alterations in breathing in normal older people," Dysphagia **17**(2), 152–161 (2002).
31. Z. A. Awan, E. Häggblad, T. Wester, M. S. Kvernebo, P. S. Halvorsen, and K. Kvernebo, "Diffuse reflectance spectroscopy: systemic and microvascular oxygen saturation is linearly correlated and hypoxia leads to increased spatial heterogeneity of microvascular saturation," Microvasc. Res. **81**(3), 245–251 (2011).

#241963 Received 18 Sep 2015; revised 21 Sep 2015; accepted 27 Sep 2015; published 30 Sep 2015

1. Introduction

The blood supply to a surgically-treated organ is the key factor in determining how well it heals and whether or not normal function will be restored. Insufficient perfusion of oxygenated blood can result in ischaemia [1] and subsequent damage to the tissue. Creation of an anastomosis (surgical attachment of two luminal structures) in the gastrointestinal (GI) tract to restore continuity following tumour resection is one such example. The local blood supply is compromised by the resection, meaning that selection and preparation of the tissue for anastomosis are important factors in ensuring the success of the procedure. Reperfusion of tissues following periods of ischaemia may result in damage to the parenchyma and the microcirculation in a condition known as ischemia-reperfusion injury [2]. Choosing the optimum surgical strategy is not always trivial however, particularly in upper GI (oesophageal) surgery, where the native blood supply is more tenuous. Failure to choose adequately perfused tissues for anastomosis may result in dehiscence of the join and leakage of GI contents, resulting in severe complications for the patient [3] including death. Intraoperative decision-making in this regard is still typically based on subjective measures, such as the appearance (colour) of the tissue, and is dependent on the experience of the surgeon.

Biophotonic imaging techniques using exogenous fluorescent agents have been proposed to monitor perfusion in the small bowel [4] but these require injection of a dye and the use of additional specialist excitation light, fluorescence filters and a sensitive, low-noise camera. Spectral imaging techniques that monitor endogenous molecules by measuring wavelength-dependent changes in diffusely-reflected light have been reported in the literature for the visualisation and quantification of the content of various biological tissues, as well as detection of abnormal tissue [5]. This includes melanin, water [6] and haemoglobin [7–9]. Internal organs are dominated by the signal from haemoglobin in the blood, whose absorption spectrum changes shape depending on whether or not oxygen is attached. This well-known property has been exploited to measure changes in oxygen saturation in tissues such as the skin [10], retina [11], brain [12] and kidney (during open surgery) [13]. Spectral imaging has also been used to investigate the effects of ischaemia-reperfusion injury [2]. The relative concentrations of oxygenated and deoxygenated haemoglobin can be determined using a simple linear spectral unmixing model [14–16], diffusion theory [17], inverse Monte Carlo [18] or a non-model-based approach [19].

Alternative techniques to quantify tissue optical properties include spatial frequency domain imaging (SFDI), which uses measurements of the modulation depth of structured light to extract and separate the absorption and scattering coefficients [20]. This technique faces challenges in registration of the multiple spatial frequency images required to form the processed image, as well as the need for synchronised projection and detection optics, which currently limit its use to open surgery.

In this paper a laparoscopic multispectral imaging system capable of following changes in tissue oxygenation intraoperatively is described and validated. The system is capable of providing high spatial resolution images of oxygen saturation and blood volume, and is compatible with open or minimally invasive procedures. Results obtained from abdominal surgeries in pigs are presented to demonstrate its correlation with blood gas measurements, and its response to dynamic oxygenation changes.

2. Materials and methods

2.1 MSI laparoscope

The MSI laparoscope hardware, which uses a similar construction to that shown by Zuzak [21], has been introduced previously [22, 23] and is shown in Fig. 1. It consists of a 30° laparoscope (Karl STORZ GmbH, Tuttlingen, Germany), liquid crystal tunable filter (LCTF; Varispec, CRi, Inc., USA), 50 mm focal length achromatic imaging lens (Thorlabs Ltd., UK)

#241963 Received 18 Sep 2015; revised 21 Sep 2015; accepted 27 Sep 2015; published 30 Sep 2015

and monochrome camera (DCU223M; Thorlabs Ltd., UK). Illumination is provided by a standard xenon surgical light source (Xenon 300; Karl STORZ GmbH, Tuttlingen, Germany). The filter, which has a scanning range between 400 and 720 nm, is controlled synchronously with the camera by a custom-written LabVIEW program (National Instruments, USA) through two USB interfaces. The system is held by an adjustable arm that allows it to be positioned statically on a trolley at the bedside.

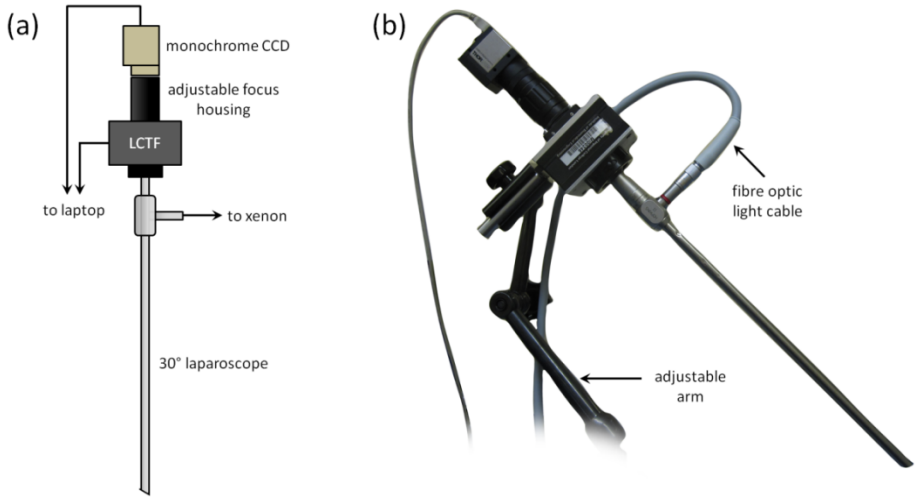

Fig. 1. Laparoscopic MSI system. (a) Schematic showing the main constituents, including the 30° laparoscope, liquid crystal tuneable filter, camera and focusing optics. (b) Photograph of the laparoscope mounted on an adjustable arm and connected to the xenon light source *via* the fibre optic light cable.

Acquisition of a full multispectral data cube involved scanning the filter from 500 to 620 nm in 10 nm steps. Exposure times needed were approximately 200 ms per image due to strong absorption by blood and the low throughput of the LCTF. Allowing for the switching time of the filter (approximately 50 ms) and image writing time, a framerate of 2 Hz was achieved. This means that almost 7 s was required for each acquisition, during which time motion artefacts from breathing and peristalsis became apparent.

Compensation for motion-induced misalignment was carried out by employing a feature-tracking image warping algorithm [12]. This algorithm works by firstly identifying a sparse set of contrast-based features in the first (reference) image in a sequence. A triangular mesh is then applied to the second (test) image and the corresponding locations of the features are then located. These matched features are then moved to align with the reference set, deforming the mesh and its constituent pixels in the process. Performance of the algorithm was optimised empirically by adjustment of the number of nodes and the rigidity of the connections. The accuracy of the algorithm has been evaluated on synthetic and experimental data in a separate publication [24], validating its performance under a variety of illumination and image noise conditions.

The motion-compensated data cube is processed to extract relative haemoglobin concentration values using a routine written in Matlab (The MathWorks, Inc., USA). This includes the initial pre-processing step of applying a spatial averaging filter (5 × 5 pixel Gaussian kernel). Assuming that the optical properties of a sufficiently small area of tissue are constant a group of neighbouring pixels in an individual wavelength image can be expected to have the same greyscale value. Averaging over these groups of pixels therefore reduces the influence of random electrical noise on the intensity of each point in the corresponding spectrum. The greyscale intensity value at pixel location (i,j) is located in each image to form a graph of intensity (I) against wavelength. This is converted to reflectance by

#241963 Received 18 Sep 2015; revised 21 Sep 2015; accepted 27 Sep 2015; published 30 Sep 2015

normalising by the corresponding reflected intensity averaged over the surface of a standard target (Spectralon; Labsphere, Inc., USA) placed at the same working distance as the tissue to be measured. This single reference spectrum is used to correct the spectra at all (i,j) locations. To remove the effect of ambient light a 'dark spectrum' (I_D) was also recorded with the xenon light switched off. The reflectance spectrum (R) was then calculated as indicated in Eq. (1):

$$R(i,j,\lambda) = \frac{I(i,j,\lambda) - I_D(i,j,\lambda)}{I_0(\lambda) - I_D(\lambda)}, \tag{1}$$

where I_0 is the reference intensity. Reflectance was converted to absorbance using Eq. (2):

$$A(i,j,\lambda) = -\ln\left(R(i,j,\lambda)\right). \tag{2}$$

A linear model of light interaction was used to interpret the reflected light signal [9, 14, 16]. This is built on the assumptions that: 1) blood is the dominant absorber in the field-of-view, 2) each wavelength travels an equal pathlength in the tissue, and 3) scattering losses are approximately equal across the wavelength range of interest. This allows an equation to be written describing attenuation of the incident light in Eq. (3):

$$A(i,j,\lambda) = [HbO_2]\varepsilon_{HbO_2}(\lambda) + [Hb]\varepsilon_{Hb}(\lambda) + \alpha, \tag{3}$$

where $[HbO_2]$ and $[Hb]$ are the concentrations of oxy and deoxyhaemoglobin, respectively, $\varepsilon(\lambda)$ is the molar extinction coefficient of each haemoglobin species, and α is a constant to account for losses due to scattering and other chromophores. A linear least squares regression algorithm was used to determine the concentrations of haemoglobin for each measured absorbance spectrum, using the known values of ε for haemoglobin [25], along with the variable α. Calculations that resulted in negative concentration values were labelled as '0' and omitted from further analysis. Measures of total haemoglobin (Hbt), which is an indicator of blood volume, and oxygen saturation (StO_2) were subsequently calculated using Eq. (4):

$$Hbt = HbO_2 + Hb;\ StO_2 = \frac{HbO_2}{Hbt}. \tag{4}$$

This procedure was repeated for each pixel location to form a complete StO_2 image. For each spectrum a measure of the quality of fit of the model was determined by calculating the coefficient of determination (CoD). Results from spectra with CoD values less than 0.9 were rejected and the corresponding pixel in the StO_2 image labelled '0' and eliminated from further calculations. For display purposes and ease-of-orientation, an RGB image was generated by integrating the reflected intensity values at each wavelength under the known transmission curves of a standard colour camera (DCU224; Thorlabs Ltd., UK), which had been measured separately. This resulted in three individual colour planes (X), as shown in Eq. (5):

$$X_F = \sum_{\lambda=460}^{\lambda=700} I(\lambda)T_F(\lambda), \tag{5}$$

where F refers to the filter of the colour plane of interest (red, green or blue), and $T_F(\lambda)$ is the corresponding transmission spectrum of the filter. For display purposes the StO_2 data was overlaid on this reconstructed RGB image, with its transparency weighted by the Hbt image. A blue/green colour map was chosen to avoid confusion with the underlying tissue colour.

2.2. Validation study

The spectral accuracy of the system was first validated on a calibrated standard colour target (ColorChecker Classic; X-Rite, Inc., USA). The reflectance spectra of 13 panels, with peaks spanning the visible range, were imaged, along with corresponding measurements from a high

#241963 Received 18 Sep 2015; revised 21 Sep 2015; accepted 27 Sep 2015; published 30 Sep 2015

resolution spectrometer (USB4000HR, Ocean Optics, Inc., USA). The reflectance spectra calculated by both methods showed strong agreement, with an average difference of 2.3%.

To validate the correspondence between tissue StO_2 measured by the MSI laparoscope and actual blood oxygen saturation an *in vivo* experiment was conducted during open abdominal surgery on a 45 kg domestic white pig. MSI readings of a section of small bowel were made immediately prior to removal of a small blood sample from the tissue. This sample was then used to fill a microfluidic cartridge for a portable blood gas analyser (i-STAT 1, Abbott Point of Care, Inc., USA), which is a clinically-approved system with validated agreement with auto-calibrated benchtop blood chemistry systems [26]. Blood was withdrawn from a vessel in the mesenteric supply as indicated in Fig. 2 (c). To induce ischaemia in the tissue windows were created in the mesentery (Fig. 2 (d)) and the vessels occluded for up to 15 minutes with rubber-shod clamps. Different segments of small bowel were used for each pair of MSI/blood gas measurements.

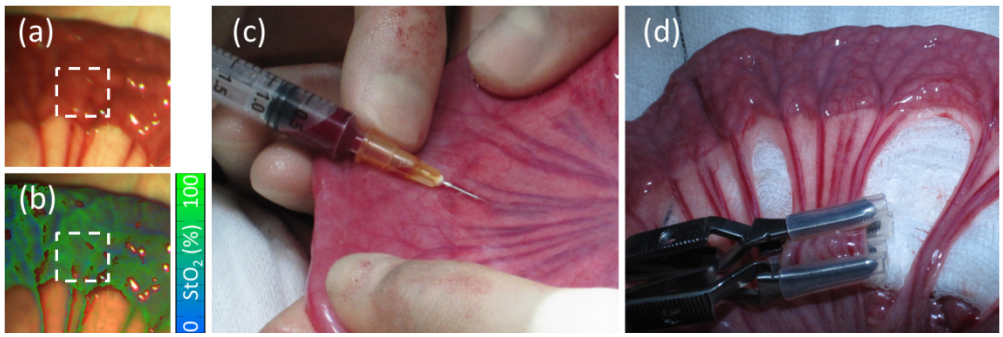

Fig. 2. Oxygen saturation validation. MSI readings were made of the small bowel serosa ((a) RGB, (b) processed StO_2 map following motion correction, as shown in Visualization 1), followed by withdrawal of a blood sample (c) from a neighbouring mesenteric vessel. The mean StO_2 of the region-of-interest (ROI), indicated by the dashed box, was then calculated. Areas of ischaemia were generated by clamping the mesenteric vessels (d).

Regions-of-interest (ROIs) from an approximately 1 cm^2 area, where the sampled mesenteric vessel meets the bowel wall, were used to extract StO_2 statistics from the tissue for further analysis. A total of 46 paired measurements were made across nine animals. The importance of image registration is demonstrated in Visualization 1, as motion artefacts result in errors in regression and StO_2 calculation.

Further *in vivo* tests were carried out to test the ability of the device to follow temporal changes in tissue oxygenation. A segment of bowel was imaged over successive periods of 15 minutes while two neighbouring groups of vessels in the mesenteric arcade were clamped and released in a manner similar to that shown in Fig. 2(d). A baseline set of measurements was recorded for five minutes before application of two rubber-shod bulldog clamps to the first group of vessels. Two more rubber-shod bulldog clamps were applied to the second, neighbouring, group after 15 minutes. The first set was then removed followed by the second set, each in 15 minute intervals. Bowel oxygen saturation was also monitored during euthanasia of one animal.

Finally the system was used in a minimally invasive surgical procedure to assess usability and performance under MIS conditions. In this case the laparoscope was inserted through a standard 10 mm trocar into the CO_2-inflated abdomen to image the large bowel.

3. Results

3.1 Error analysis: uncertainty estimation

A repeatability study was carried out by acquiring successive images of a single segment of porcine small bowel under resting conditions, where no external stimuli were used to cause

#241963 Received 18 Sep 2015; revised 21 Sep 2015; accepted 27 Sep 2015; published 30 Sep 2015

any change in StO_2. Within the resulting sequence of saturation images the standard deviation of a spatial pixel (i,j) in the temporal dimension was calculated. Repeating this calculation for every pixel resulted in the map of temporal standard deviation (σ^{t}_{StO2}) shown in Fig. 3(a). The distribution of values (Fig. 3(b)) shows a peak at 7.5%. There is also a spatial variation in StO_2 in any given patch on the bowel wall. To quantify this large ROI (160 × 160 pixels; ~1 cm^2) was defined on a processed image of a healthy bowel segment. Within this area a smaller, square sub-ROI was placed and the standard deviation measured. This was repeated with the sub-ROI placed in a total of 30 randomly-selected locations within the larger ROI. The average of these measurements is a measure of the spatial standard deviation (σ^{s}_{StO2}) for that sub-ROI size. This process was repeated for varying sub-ROI sizes to reveal relationship between ROI size and σ^{s}_{StO2}, as shown in Fig. 3(c).

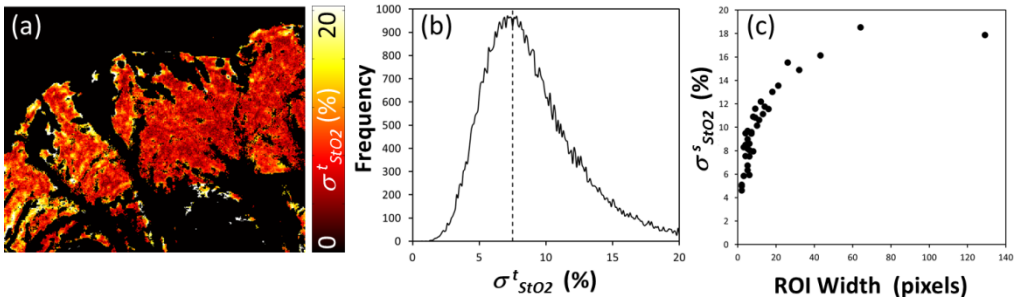

Fig. 3. Temporal and spatial variation. (a) Map of σ^{t}_{StO2} in a segment of bowel over seven acquisitions. (b) Histogram of σ^{t}_{StO2} recorded over the entire bowel segment. (c) Spatial standard deviation of StO_2 values (σ^{s}_{StO2}) as the ROI size is varied.

The average measured temporal variation in StO_2 was 7.5%. Artefacts due to motion between acquisitions were not corrected, due to the difficulty in registering the comparatively noisier processed StO_2 images, so it is expected that the actual uncertainty on a given measurement would be lower than that figure, and it is likely that the saturation was varying as a function of time. Spatial variation of oxygenation is much larger (18%) within a large ROI but is seen to decrease and reaches a level close to that of the temporal variation as the ROI approaches the spatial resolution of the device (5 × 5 pixels). Over the entire data set, excluding regions where confounding specular highlights were present, an average of 4.7% of pixels were eliminated for having CoD values below the threshold.

3.2 Validation: MSI vs. blood gas

The results of the validation study, consisting of 46 paired measurements, are shown in Fig. 4. The scatter of points shows that the MSI laparoscope is capable of detecting changes in oxygen saturation in the 30-100% range. The Pearson correlation coefficient between the two measurements is 0.76.

#241963 Received 18 Sep 2015; revised 21 Sep 2015; accepted 27 Sep 2015; published 30 Sep 2015

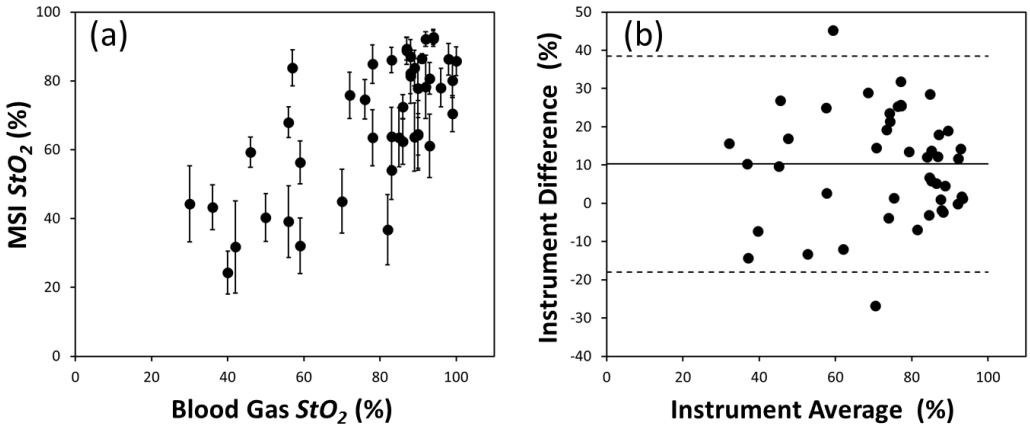

Fig. 4. (a) Plot of mean StO_2 from the selected MSI ROI against oxygen saturation in the neighbouring vessel measured by the blood gas analyser. The error bars indicate ± 1 standard deviation (σ) of StO_2 values within each ROI. (b) Bland-Altman plot, showing the absolute difference between the MSI and blood gas instruments as a function of their mean value. Horizontal lines indicate the absolute mean difference ± 1.96σ.

A Bland Altman analysis of the difference in StO_2 measured by the MSI laparoscope and the blood gas analyser, shown in Fig. 4(b), indicates an RMS difference of 18% between the devices. The scatter of points is approximately even about the mean, with a slight positive gain of 0.01.

3.3 Occlusion studies

The variations in tissue oxygen saturation during clamping of sections of the mesenteric arcade are shown in the StO_2 images and ROI time plot in Fig. 5. High baseline saturation values (mean value of 78 ± 1% over the initial 5 min) are noted prior to clamping and are visible as bright green areas in the processed MSI image. A timelapse animation of the entire data set is visible in Visualization 2.

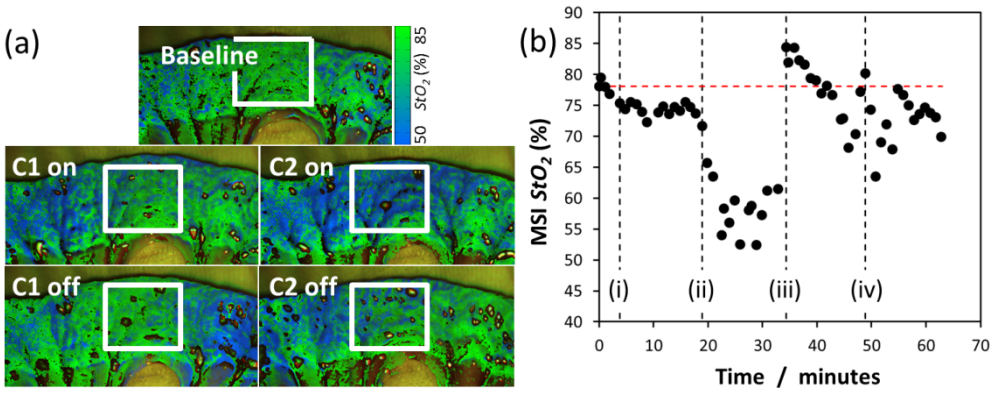

Fig. 5. Variation of StO_2 with time (Visualization 2) during successive clamping and release of segments of porcine small bowel. (a) Processed StO_2 images of the bowel at each of the five distinct stages during the experiment as clamps (C1 and C2) were applied ('on') and released ('off'). (b) StO_2 in a region of interest located in the centre of the bowel segment (white box) in the images shown in (a). The black dashed lines represent time-points for (i) C1 on, (ii) C2 on, (iii) C1 off and (iv) C2 off, while the red dashed line indicates the average baseline saturation.

The StO_2 overlay images in Fig. 5(a) show that almost 15 minutes after application of the first clamp (C1; Fig. 5(b)(i)) an area of ischaemia (blue colour) has developed in the left-hand side and the mean saturation of the ROI drops slightly to 75 ± 1%. When the second clamp

#241963 Received 18 Sep 2015; revised 21 Sep 2015; accepted 27 Sep 2015; published 30 Sep 2015

(C2) is applied alongside C1 this ischaemic area spreads across the bowel segment as most of the supply to the tissue is now occluded, and saturation drops sharply to 57 ± 3% (Fig. 5(b)(ii)). A marked recovery is seen in both sides of the bowel after each clamp is removed, although saturation levels remain slightly ischaemic on the left-hand side with respect to the baseline image. The mean StO_2 value increases rapidly to a level greater than baseline levels (~84%; Fig. 5(b)(iii)) after the release of C1 and settles slowly over a period of approximately 10 minutes, during which there is a high degree of scatter (Fig. 5(b)(iv)). The final saturation value is close to, but lower than, baseline levels (74 ± 2%).

At the end of one procedure the MSI laparoscope was used to track StO_2 in a loop of small bowel over a period of 8 minutes as the animal was euthanised. The time course of the oxygenation changes can be seen in the StO_2 maps (Fig. 6(a) and Visualization 3), with the colour changing visibly from bright green to dark blue. The mean saturation values in Fig. 6(b) show a decrease within one minute of administration of the drug. At the four-minute mark the tissue StO_2 has dropped to just over 30%. The decrease in saturation is visible in the processed saturation maps (Fig. 6(a) and Visualization 3) with the tissue changing visibly from bright green to dark blue.

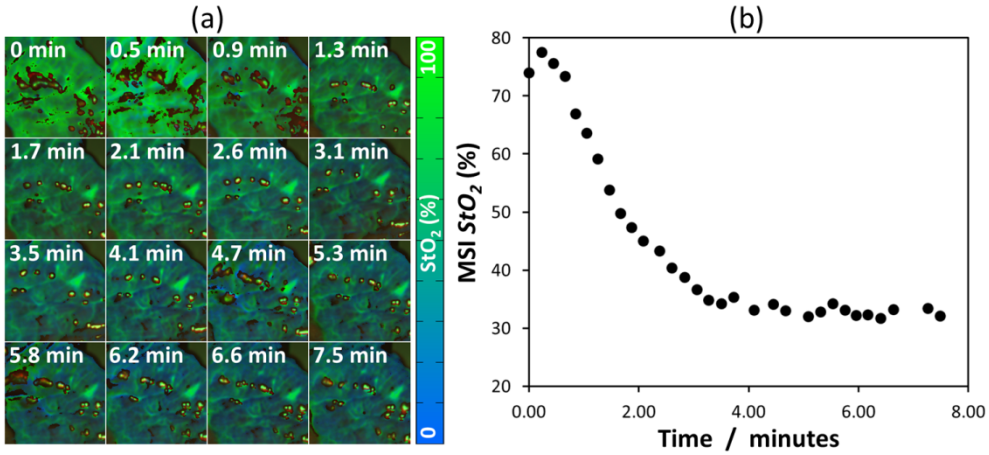

Fig. 6. Oxygen saturation following delivery of drugs to euthanise the porcine test subject (a) StO_2 maps as a function of time. (b) Mean StO_2 of bowel wall ROI (Visualization 3).

In the MIS procedure the laparoscope was able to successfully visualise spatial variations in oxygen saturation in the bowel wall. Average baseline values of 78% were obtained.

4. Discussion

The MSI laparoscope presented in this paper has demonstrated sensitivity to changes in tissue oxygen saturation in a series of *in vivo* porcine bowel imaging experiments. The validation result (Fig. 4) shows a correlation between the MSI-measured tissue oxygenation and the blood gas analyser-measured mesenteric saturation. The MSI result tends to be lower than the corresponding blood gas analysis result (just over 10% on average), and there is also a visible amount of scatter in the data, as well as uncertainty in each individual MSI point. The tissue motion has been accurately corrected by the feature-tracking image warping algorithm, which is essential in the case of the 7 second total time required for the sequential image acquisition. We note that such a correction would still be required for faster acquisition rates due to the variable speed of the respiratory motion across the respiratory cycle, and also for image fields that are affected by the cardiac cycle. For total acquisition times of less than 100 ms respiratory or cardiac gating could be proposed.

#241963 Received 18 Sep 2015; revised 21 Sep 2015; accepted 27 Sep 2015; published 30 Sep 2015

4.1 Model assumptions

A simple linear model of light attenuation in tissue was used to calculate the relative contributions of oxy and deoxyhaemoglobin to the measured absorbance spectrum at each location in the tissue. This includes assumptions that, over the wavelength range of interest, the scattering spectrum is flat, the pathlength travelled is equal for all photons, and haemoglobin is the dominant optical absorber. The advantage is that the resulting model, described by Eq. (3), may be rapidly solved for the three unknowns, making it suitable for use in an image processing application. The reduced scattering spectrum of tissue has been shown to follow the empirical relation $\mu'_s = a\lambda^{-b}$, where the a and b parameters represent a scaling factor and scattering power, respectively [27]. Over the 120 nm range used in this work μ'_s could be expected to decrease by approximately 4 mm^{-1} (20%), based on previously obtained values for the bowel [27]. Furthermore the mean geometrical pathlength travelled by each wavelength, which is determined by the penetration depth, has been shown to vary across the visible spectrum. Measurements of cortical diffuse reflectance spectra have estimated that the differential pathlength factor at 620 nm is approximately 2.5 times greater than at 500 nm [28]. This means that calculated absorbance may be overestimated at the red end of the spectrum (λ > 600 nm) as it is proportional to the pathlength travelled by the photon.

4.2 Dynamic clamping experiments

The StO_2 images in Fig. 5(a) demonstrate how the bowel tissue is supplied by mesenteric vessels. Clamping of one group of vessels results in a measured drop in saturation in the neighbouring tissue, as might be expected, but some areas of the bowel close to the clamped vessels remain oxygenated. This is expected due to a supply of oxygenated blood reaching the bowel wall by marginal vessel arcades that run parallel to the mesenteric border of the bowel wall, which are in turn fed by unaffected mesenteric vessels. Therefore when a neighbouring group of vessels is fully clamped from immediately below the mesenteric border the ischaemic region spreads between and beyond the two occluded segments.

The degree of variability in StO_2 evident in Fig. 5(b) may also be explained with reference to the marginal vessels. Following the application of C2, and the immediate hypoxia that results, venous congestion commences. This leads to patchy ischaemia within the ROI, with variable haemodynamics from capillary collaterals [(ii)-(iii)]. Once perfusion is restored by removing C1 (iii), there is a visible reactive hyperaemia and venous pressure gradually increases secondarily to clear the built-up metabolites. Thus, venous congestion and the resulting tissue oedema is much slower and variable in its recovery once the final clamp is removed. All of these factors lead to a natural degree of variability in StO_2 as the gradual recovery process ensues.

4.3 Heterogeneity and scatter

The temporal variation in the StO_2 measurement was found to be ± 7.5%. This is a combination of instrument noise and physiological temporal fluctuations in oxygenation. The first source is caused by uncertainty in the measured absorbance spectrum, due to thermal noise in the CCD in low signal areas (high absorption or poor LCTF throughput), which in turn led to errors in regression and the evaluation of Eq. (3) as well as the negative saturation values that were sometimes calculated. With regard to physiological variations previous studies have demonstrated changes in systemic StO_2 as a result of surgery [29], and even changes of 2-4% while swallowing in some cases [30].

The i-STAT blood gas analyser used in the validation experiment is also subject to deviations due to changes in body temperature. This is due to the fact that the instrument calculates oxygen saturation from directly measured partial oxygen pressure and pH. A correction term, supplied by the manufacturer, shows that when body temperature deviates from the calibration value of 37°C the calculated saturation also deviates. This means that a

#241963 Received 18 Sep 2015; revised 21 Sep 2015; accepted 27 Sep 2015; published 30 Sep 2015

2°C drop would result in saturation being over-estimated by 3% at an StO_2 instrument reading of 90%, and as much as 9% at an StO_2 instrument reading of 40%.

When examining mean values of oxygen saturation from StO_2 images it was noticed that the standard deviation of the values could be as high as 18% (StO_2) over a large (~1 cm^2) area but would decrease and tend towards the expected temporal variability as the size of the ROI decreased toward the limit of the imager's spatial resolution. Therefore it is suggested that this higher variation may originate from real spatial heterogeneity in the measurement due to physiological variability within a given volume. This has been demonstrated previously in diffuse reflectance measurements on the skin, which showed the highly heterogeneous nature of the microvasculature and the resulting spatial variations in oxygen content that may be present [31].

Another source of scatter in the StO_2 validation plot arises from uncertainty over the composition of the microvasculature in the bowel wall, which, depending on the location of the ROI, may be primarily venous, arterial or a mixture of both. Differentiating arteries from veins in the mesenteric arcade was non-trivial, and could only be confirmed following the blood gas measurement. Therefore it may be possible that a blood sample was taken from an artery but the ROI was from a mainly venous area of tissue. This effect would also explain occasions when the imager returned lower values than blood gas analysis at high oxygen saturations and *vice versa*.

Further scatter in the data may be due to inter-subject variability, as the validation experiment was conducted at 46 separate tissue sites over nine animals. Differences in illumination conditions, small variations in working distance and laparoscope pose, and tissue optical properties may be expected to contribute to this variability.

5. Conclusions

A laparoscopic multispectral imaging system incorporating motion-correction software has been shown to be sensitive to changes in tissue oxygenation during surgery and can follow changes temporally. Absolute values of oxygen saturation in the tissue, as measured by the imager, are correlated to the blood oxygen saturation from a supplying vessel as measured by a clinical blood gas analyser. Images of tissue undergoing dynamic occlusion demonstrated its ability to map the spatial extent of ischaemia.

Inter-subject variability was found to influence absolute measurements, contributing to a large amount of scatter in the validation study. Within a single test subject however temporal fluctuations in StO_2 were found to be ± 7.5%. The distribution of StO_2 values with large ROIs (~1 cm^2) show variability greater than that of the instrument, indicating the presence of real, physiological heterogeneity.

Future work will include algorithmic improvements that incorporate a more realistic model of light-tissue interaction. Simulation of photon propagation in bowel tissue using Monte Carlo modelling will be used to estimate a differential pathlength factor that can compensate for wavelength-dependent variations in penetration depth, while the 'flat' scattering term (α) will be replaced by an empirical power law. Implementation of these changes will also require more time-efficient processing strategies to offset the higher computational cost.

A more clinically feasible real-time system is currently being developed through improvements in image acquisition hardware, software design, and algorithm implementation. Preliminary work in data reduction techniques and non-model-based approaches to StO_2 prediction have demonstrated the feasibility of using a fast filter wheel system with fewer wavelengths [19]. This hardware would enable a decrease in acquisition time from 7 s to approximately 0.3 s, meaning that respiration and peristalsis-related motion artefacts would be greatly reduced. The registration algorithm would be capable of resolving this range of motion in real-time [24].

#241963 Received 18 Sep 2015; revised 21 Sep 2015; accepted 27 Sep 2015; published 30 Sep 2015

Clinical applications of this laparoscope are currently being pursued and focus on assessment of perfusion in the GI tract following anastomosis surgery. Studies of acute and longer-term changes in StO_2 in the perianastomotic region following surgery in animals will be used to compare the effectiveness of different surgical techniques.

Acknowledgments

Funding for this work was provided by ERC grant 242991. Neil Clancy would like to gratefully acknowledge the financial support of an Imperial College Junior Research Fellowship. Shobhit Arya is supported by an NIHR-HTD 240 grant. The authors would like to thank the Northwick Park Institute for Medical Research for their assistance with surgical arrangements. The surgical procedure was conducted under UK Home Office personal animal licence (PIL) No. 70/24843 and project licence (PPL) No. 8012639.

#241963 Received 18 Sep 2015; revised 21 Sep 2015; accepted 27 Sep 2015; published 30 Sep 2015